Supplementary Information

Ultrasmall $FeNiP_x$ nanoparticles embedded into amorphous $FeNiO_x$ nanosheets for industrial-level high current density water oxidation

Ashish K. Yadav,[a] Parvez A. Khan,[a] Anirudha Shekhawat,[b] Jeyakumar Karthikeyan,[c] Harish Hirani,[d] Wolfgang Schuhmann,[b] and Arshad Aijaz*[a]

[a]Department of Energy & Human Sciences, Rajiv Gandhi Institute of Petroleum Technology (RGIPT) – Jais, Amethi, Uttar Pradesh-229304, India. Email: aaijaz@rgipt.ac.in

[b]Analytical Chemistry–Center for Electrochemical Sciences (CES), Faculty of Chemistry and Biochemistry, Ruhr University Bochum, Universitätsstraße 150, D-44780 Bochum, Germany.

[c]Department of Physics, National Institute of Technology, Durgapur-713209, West Bengal, India.

[d]Department of Mechanical Engineering, Rajiv Gandhi Institute of Petroleum Technology (RGIPT) – Jais, Amethi, Uttar Pradesh-229304, India.

1. Chemicals

All chemicals and reagents used in this work were directly purchased with >99% purity. Ferric Nitrate nonahydrate ($Fe(NO_3)_3.9H_2O$) analytical grade (A.R.) was purchased from Merck. Sodium sulphide ($Na_2S.9H_2O$) Iron-free (A.R.), was purchased Molychem. Sodium hypophosphite monohydrate ($Na_2H_2PO_2$) and Nickel Foam (NF) was purchased from Sigma-Aldrich. Ethanol was obtained from Changshu Hongsheng Fine Chemicals Ltd. The Hydrochloric acid was purchased from Finar chemicals. Milli Q-ultrapure water (resistance of 18.2 MΩ.cm at 25˚C) was used for synthesis process and making the electrolytic solutions except seawater electrolysis.

2. Material Characterization

2.1 Details of equipment: Powder X-ray diffraction (PXRD) was measured using Panalytical, EMPYREAN-QTY1 diffractometer having a X-Ray generator with specification of operating voltage of 220-240 V - 50 Hz, single-phase rated voltage of 20-60 kV or better, anode current 2-60 mA with 2°/min scan rate and 0.0625 steps. X-ray photoelectron spectroscopy (XPS) was performed on a Thermo-Fisher Scientific (K-Alpha) X-ray photoelectron spectrometer having an Al Kα source (10 kV, 10 mA) equipped with an ion source (EX06). Ar sputtering experiments were carried out under the conditions of background vacuum ~10^{-8} Pa, sputtering acceleration voltage was kept 2 kV and sputtering current at 10 mA. Ar sputtering was performed for 120 seconds for each analysis. Scanning electron microscopy (SEM) images were acquired using JEOL (JXA-8230) operated at 20 kV. The XRD, XPS and FE-SEM analysis was done at facilities of CIF, Rajiv Gandhi Institute of Petroleum Technology (RGIPT), Jais. Transmission Electron Microscopy (TEM) images were acquired using FEI Tecnai G2 F30 transmission electron microscope operated at 300 kV having a resolution point 2 Å and line 1 Å with a magnification power of 58 x to 1 million located at SAIF IIT-Bombay. Raman measurements were completed on either Princeton Instruments Acton Spectra Pro 2500i having a 532 nm DPSS Laser (Laser Quantum gem 50 mw) or JASCO NRS 5500 Laser Raman Spectrometer. Atomic Force Microscopy (AFM) analysis was done with the help of MFP-3D BIO Asylum Research, USA in tapping mode at SAIF IIT-Bombay.

2.2 Measurement of d-band centre: The valence band spectra were acquired using a XPS equipment with Al Kα source (10 kV, 10 mA) equipped with ion source (EX06). Survey scans were recorded with an X-ray source power of 150 W and a pass energy of 100 eV. Major elements were recorded at 20 eV pass energy. The binding energy was referenced to the C 1s peak at 284.8 eV and the ratio of Lorentzian to Gaussian was 0.2. The surface valence band photoemission spectra (VB-XPS) were processed by subtracting the Shirley background. To ensure accurate comparison across all valence band spectra, the upper limit for background integration was consistently set at a binding energy of 16.0 eV.

The d-band centre was determined using the formula:

$$c = \frac{\int N(\varepsilon) \,.\, \varepsilon \, d\varepsilon}{\int N(\varepsilon) \, d\varepsilon}$$

Where, N (ε) and ε are the density of states and binding energy, respectively.

3. Electrochemical measurements

All the electrochemical measurements were executed on Biologic VSP-128 Potentiostat and EC-lab workstation at room temperature. The electrodes were tested in a typical 3-electrode system using 1M KOH aqueous solution. The Hg/HgO (1M NaOH) was selected as reference electrode, a wired platinum mesh was used as counter electrode and the prepared electrocatalysts were taken as the working electrodes without using any binder material. The cyclic voltammetry (CV) and linear sweep voltammetry (LSV) measurements were performed at scan rate of either 1 or 5 mV s^{-1}. The exchange current density was derived by extrapolating the Tafel curve directly obtained from EC-lab software. The electrochemical impedance spectroscopy (EIS) measurements were recorded in the frequency region of 10^5 Hz to 10^{-2} Hz with the amplitude of 5 mV at various potentials. The electrochemical active surface area (ECSA) was determined using CV techniques which were recorded at the various scan rates from 20 to 120 mV s^{-1}. The ΔJ was calculated by taking difference of J_{anodic} and $J_{cathodic}$. Stability measurements were performed using the Chronopotentiometric method. When KOH was added to seawater, collected from beaches of the Bay of Bengal, it formed a white turbid solution. Before use, it was filtered with normal filter paper and pH was determined/maintained using a pH meter. All the recorded potential were converted w.r.t. to RHE using the formula:

$$\mathbf{E_{(RHE)} = E_{Hg/HgO} + 0.059\ pH + E^{o}_{Hg/HgO}}$$

Turnover frequency (TOF) and number of active sites were determined by CV techniques in phosphate buffer saline solution of pH = 7, prepared by dissolving 12.4 mmol Na_2HPO_4 and 7.6 mmol NaH_2PO_4 solutions in deionised water. CV were collected by keeping the scan range between -0.2 V to 0.6 V vs RHE with a scan rate of 50 mV/s (Fig. S11), and number of active sites (N) was calculated using:

$$N = \frac{I * V/v}{2F}$$

where N is number of active sites, V is the potential vs RHE, v is the scanning rate, and F is Faraday's constant.

Furthermore, TOF was calculated using the formula:

$$TOF = \frac{j\,S}{nNF}$$

Where j denotes the current density, S surface area of working electrode (1 cm^2), N is the no. of active sites derived from previous equation, F is the faraday's constant, and n is the number of electrons transferred during the reaction (here n = 4 for OER).

In addition, the faradaic efficiency was determined by collecting the evolved H_2 and O_2 gases by water displacement method in an inverted burette. The amount of observed volume of gases was converted into number of millimoles.

The theoretical amount of evolved O_2 gas (n) was calculated using the Faraday's law:

$$n = \frac{I.t}{z.F}$$

Where the I is the current in ampere, t is the time in sec, F is the Faraday's constant, and z is the number of electrons transferred (n = 4 of OER).

The experimental amount of evolved gases was calculated by water displacement method using Dalton's law: $P_{Total} = P_{O2/H2} + P_{H2O}$

Vapour pressure of water was assumed to be 21.1 mm of Hg at STP conditions. The no. of moles of O_2 and H_2 was calculated by:

$$P_{O2}\,V_{O2} = nRT \ldots\ldots\ldots (for\ OER)$$

Where V_{O2} is the volume of O_2 collected. P_{O2} is the pressure for the O_2, R is the gas constant and T is the temperature.

The Faradaic Efficiency was finally calculated by using:

$$\text{Faradaic Efficiency} = \frac{\text{Experimental moles of } O_2}{\text{Theoretical moles of } O_2} \times 100$$

For Bode analysis, the EIS measurements were recorded in the frequency region of 10^5 Hz to 10^{-2} Hz with the amplitude of 5 mV at various potential ranging from 1.4 V to 1.5 V vs RHE. The obtained Nyquist Impedance graph was directly converted to Bode plots in-built EC-Lab analysis software.

In-situ Raman measurement was performed by simply using home-made 3-electrode electrolysis cell equipped with an opening and sealed with a quartz window area, large enough to focus laser on the working electrode beneath it. The wavelength of the laser was kept being constant at 532 nm

for all measurements. The spectra were recorded at different potentials from 1.3 to 1.6 V vs RHE using chronoamperometric techniques.

4. Zero-gap 3-electrode flow-through cell and water electrolyser assembly

4.1 Zero-gap 3-electrode membrane assembly: $FeNiP_x/FeNiO_x$/NF electrode was tested for the OER activity in a 3-electrode configuration MEA-type flow-through cell. A nickel foam was used as counter electrode and both electrodes were separated using an anion exchange membrane (Fumatech fumasep FAA-3- PK-130), resulting in a MEA-type configuration. The 1 M KOH electrolyte was circulated through the anode and cathode compartment separately using a peristaltic pump at a flow rate of 20 mL min^{-1}. The employed reference electrode, which is kept at a constant distance from the working electrode surface, was a Ag|AgCl|KCl (3 M) double junction electrode where the double junction was filled with 1 M KOH. The MEA was used without any hot pressing. The geometric area of the electrodes was kept at 0.95 cm^2 and the flow through the cell was tightly closed using screws with an applied torque of 0.4 Nm to prevent leakage. Electrochemical characterization was carried out at room temperature using an Autolab PGSTAT128 N with booster PGSTAT BSTR10A (Metrohm). Before measurements, the membrane was hydrated for at least 1 h in 1 M KOH. To activate the catalytic surface, a cyclic voltammogram (CV) was conducted at a scan rate of 50 $mV \cdot s^{-1}$ (50 cycles) in a potential range from 0.2 to 0.5 V vs. Ag|AgCl|KCl (3 M) before OER measurements. Constant current chronopotentiometry measurements were carried out at 1.0 $A \cdot cm^{-2}$ current density.

4.2 Alkaline water electrolyser assembly: $FeNiP_x/FeNiO_x$/NF was tested as anode in water electrolyzer assembly. $FeNiP_x/FeNiO_x$/NF and Pt/NF (as cathode) was separated with an anion exchange membrane (Sustainion X37-50 grade T, Dioxide Materials). Electrode assembly was completed using carbon cloth as gas diffusion layers (GDL), serpentine flow channels, and gaskets (for leakage proofing), typically depicted as in main text Fig. 5g. Both the anodic and cathodic chambers were provided with inlet and outlet for electrolytes (6 M KOH). A flow rate of 50 mL min^{-1} at both anode and cathode was maintained using peristaltic pumps. Anode and cathode were further connected with copper foils to complete the electrical connections. To activate the catalytic surface, a cyclic voltammogram (CV) was conducted at a scan rate of 100 $mV \cdot s^{-1}$ (20 cycles) in a potential range from 1.1 to 2 V before the LSV measurements. LSV was acquired at a scan rate of 5 mV sec^{-1}. Constant current chronopotentiometry measurements were carried out at 0.50 and 1.0 $A \cdot cm^{-2}$ current densities.

5. Computational methods

All first-principles calculations were carried out within the framework of density functional theory (DFT) as implemented in the Vienna *Ab initio* Simulation Package (VASP).[1] The interaction between valence electrons and ionic cores was treated using the projector augmented wave (PAW) method,[2] and a plane-wave cutoff of 500 eV was used to ensure accurate total energies. Exchange–correlation effects were described using the generalized gradient approximations (GGA) in the Perdew-Burke-Ernzerhof (PBE) functional.[3] Since the localized 3d states of Fe and Ni are not well represented in conventional GGA, on-site Coulomb interactions were included through the GGA+U scheme,[4] with effective U values of 5.5 eV for Fe and 6.5 eV for Ni. The electronic self-consistency criterion was set to 10^{-6} eV, and atomic structures were relaxed until the residual forces on each atom were below 0.01 eV/Å. Brillouin-zone sampling for the slab models was performed using an 8×8×1 Monkhorst–Pack k-point mesh.[5] Structural models of FeNiP and FeNiO were derived from their parent hexagonal lattices. In the case of FeNiO, Ni atoms are placed in the octahedral voids, while Fe atoms are inserted into interlayer octahedral sites. Slabs were cleaved along the (001) direction, consisting of two layers for the oxide and four layers for the phosphide. To reproduce the amorphous-like features observed experimentally in FeNiO, 2×2×1 supercells were constructed, and selected Fe atoms were substituted by Ni, resulting in a Ni: Fe ratio close to 2. This substitution was distributed across all layers to maintain both Ni and Fe, thereby increasing structural disorder. The resulting compositions were $Fe_3Ni_5O_8$ (oxide) and $Fe_4Ni_8P_6$ (phosphide). Finally, these slabs were stacked to build the $Fe_{0.66}Ni_{1.33}P/Fe_{0.37}Ni_{0.63}O$ heterostructure. For the oxide, phosphide, and heterostructure, the in-plane lattice constants were optimized in both the x and y directions, and no symmetry constraints were applied so that the interfacial relaxation could be captured realistically. The d-band center was computed following the method proposed by Nørskov and co-workers,[6] where the d-band center (ε_d) is defined as the first moment of the projected d-density of states (PDOS) relative to the vacuum potential calibrated Fermi level:

$$\varepsilon_d = \frac{\int_{-\infty}^{+\infty} \varepsilon \; n_d(\varepsilon)\, d\varepsilon}{\int_{-\infty}^{+\infty} n_d\,(\varepsilon)\, d\varepsilon}$$

Here, $n_d(\varepsilon)$ represents the projected density of d states at an energy ε, for all elements present in the surface slab. In our work, the d-band center was extracted from the atom-projected DOS of each element using the VASPKIT.[7] The integration was performed over the full energy range of the d-states, and all d-band centre energies were referenced to the work function of the respective slabs, obtained from the self-consistent DFT calculation, ensuring a consistent vacuum-level alignment across different surface models.

1 G. Kresse and J. Furthmüller, *Comput. Mater. Sci.,* 1996, **6**, 15.

2 G. Kresse and D. Joubert, *Phys. Rev. B,* 1999, **59**, 1758.

3 J. P. Perdew, K. Burke and M. Ernzerhof, *Phys. Rev. Lett.,* 1996, **77**, 3865.

4 S. L. Dudarev, G. A. Botton, S. Y. Savrasov, C. J. Humphreys and A. P. Sutton, *Phys. Rev. B,* 1998, **57**, 1505.

5 H. J. Monkhorst and J. D. Pack, *Phys. Rev. B,* 1976, **13**, 5188.

6 B. Hammer and J. K. Nørskov, *Surf. Sci.,* 1995, **343**, 211.

7 V. Wang, N. Xu, J.-C. Liu, G. Tang and W.-T. Geng, *Comput. Phys. Commun.,* 2021, **267**, 108033.

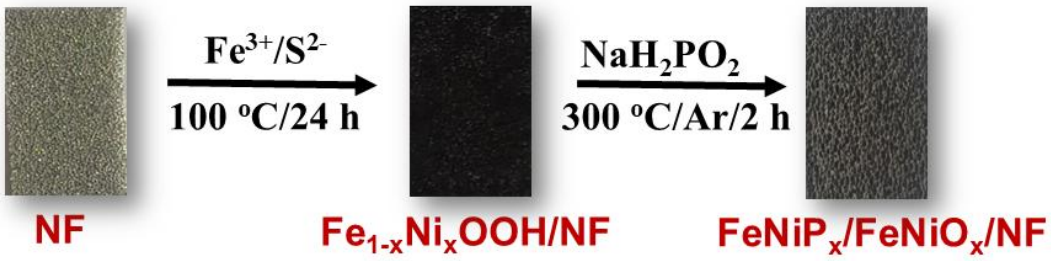

Fig. S1 Digital photographs of obtained electrodes during synthesis of $FeNiP_x/FeNiO_x/NF$.

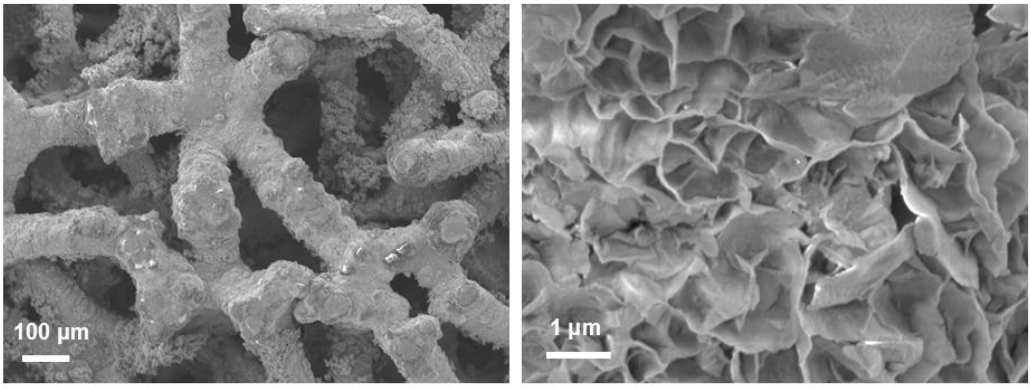

Fig. S2 SEM Images of $Fe_{1-x}Ni_xOOH/NF$ at two different resolutions.

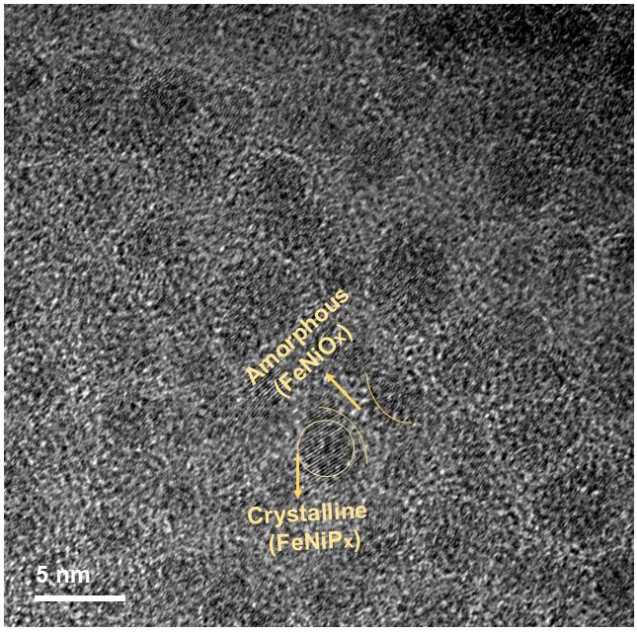

Fig. S3 Amorphous-crystalline interfaces exist in $FeNiP_x/FeNiO_x/NF$.

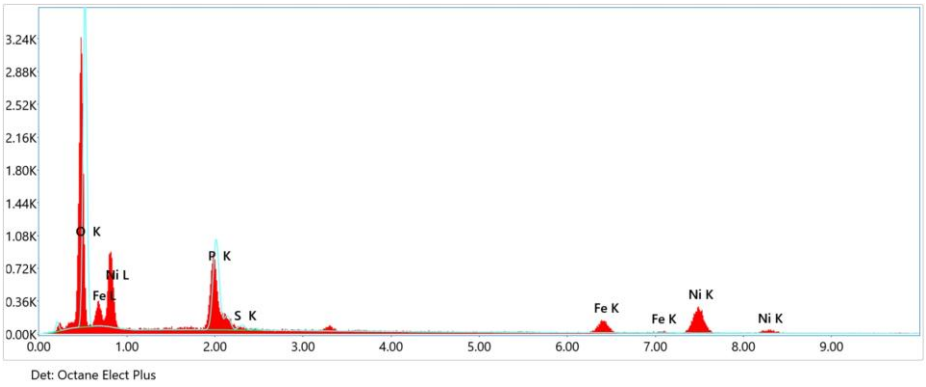

Element	Weight %	MDL	Atomic %	Net Int.
O K	38.8	0.27	65.6	986.5
P K	13.6	0.26	11.9	423.7
S K	0.8	0.27	0.7	25.0
Fe K	10.3	0.66	5.0	103.5
Ni K	36.5	1.30	16.8	210.8

Fig. S4 SEM-EDX and corresponding elemental analysis of $FeNiP_x/FeNiO_x/NF$.

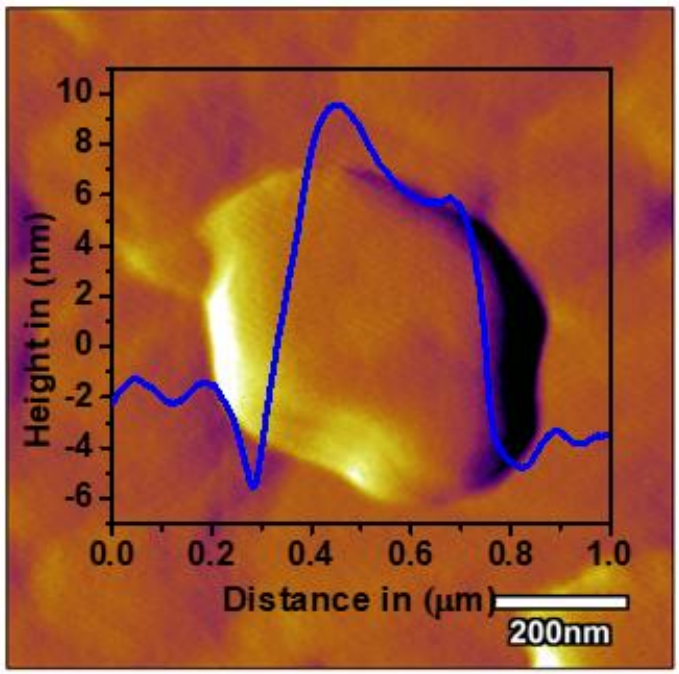

Fig. S5 AFM image of single nanosheet of $FeNiP_x/FeNiO_x/NF$.

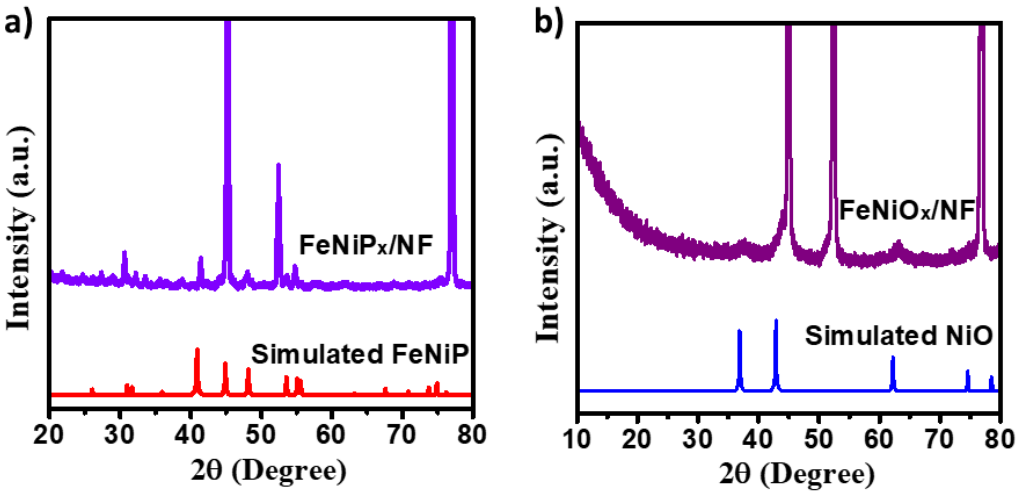

Fig. S6 PXRD patterns of (a) $FeNiP_x$/NF, and (b) $FeNiO_x$/NF samples.

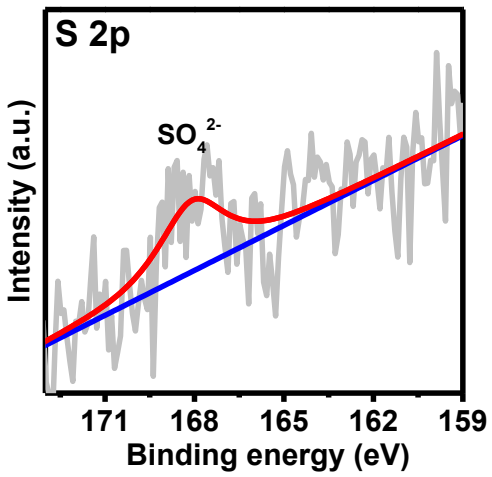

Fig. S7 High resolution S 2p XPS spectrum of $FeNiP_x$/$FeNiO_x$/NF.

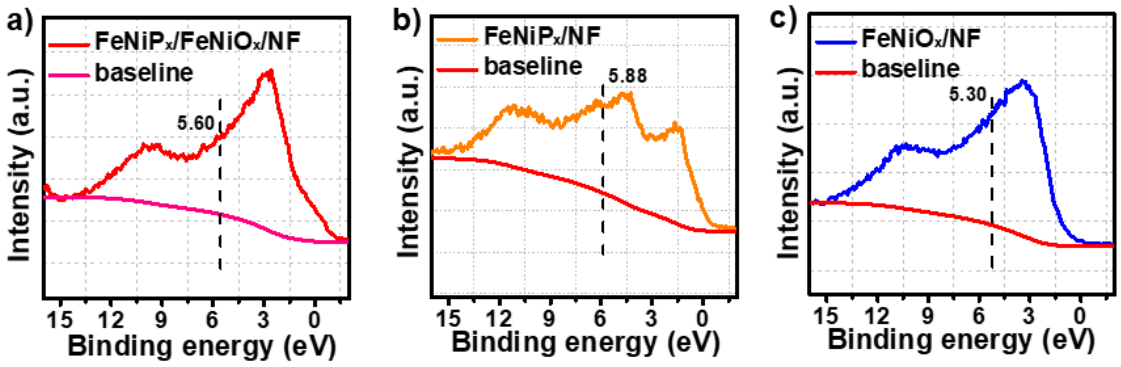

Fig. S8 Raw valance band XPS spectra of $FeNiP_x/FeNiO_x/NF$, $FeNiP_x/NF$, $FeNiO_x/NF$ for the calculation of valence band center.

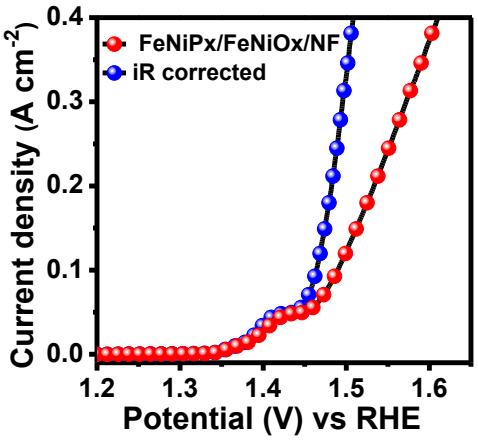

Fig. S9 Voltammograms of $FeNiP_x/FeNiO_x/NF$ for OER with non-iR-corrected (red) and 90% iR-corrected (blue) data.

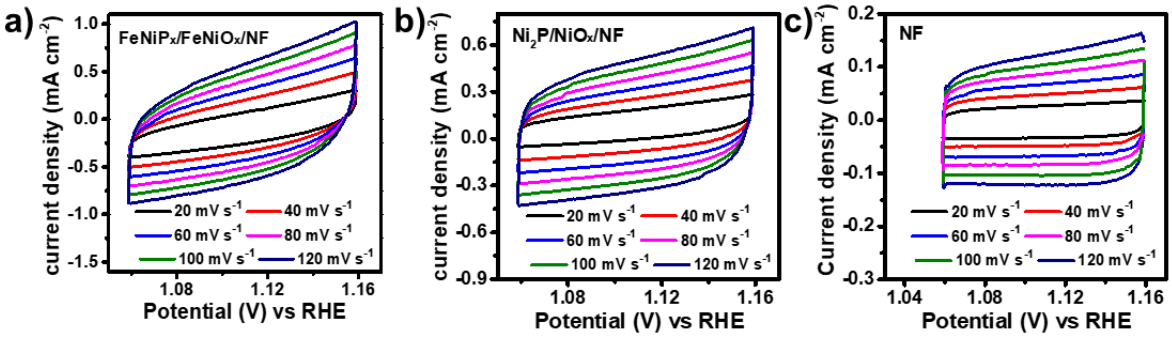

Fig. S10 CV recorded at different scanning rates of electrocatalysts for the calculations of C_{dl} during OER.

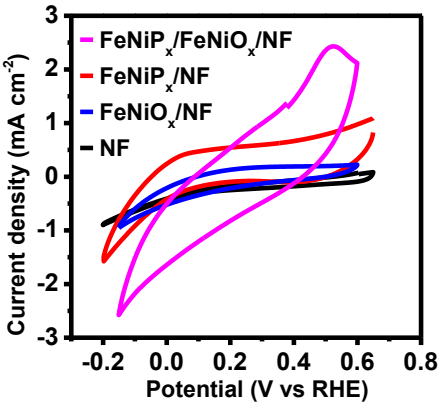

Fig. S11 CV measurements in phosphate buffer saline (pH 7) at a scan rate of 50 mV s^{-1}.

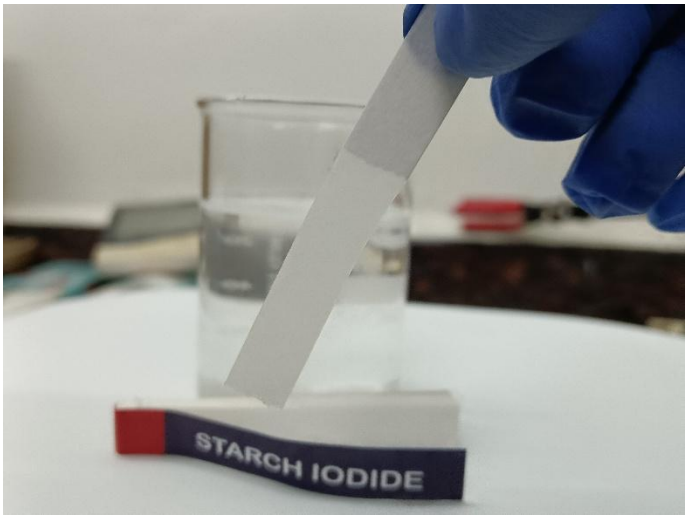

Fig. S12 Chlorine precipitation test with KI-starch paper after stability testing.

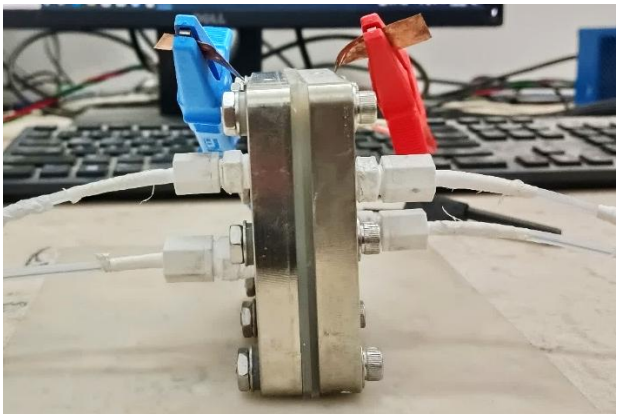

Fig. S13 Digital photograph of the assembled electrolyser.

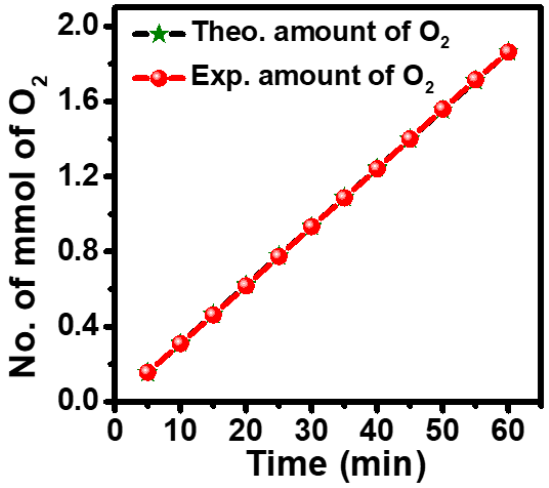

Fig. S14 Faradaic efficiency for OER determined at the current density of 100 mA cm^{-2}.

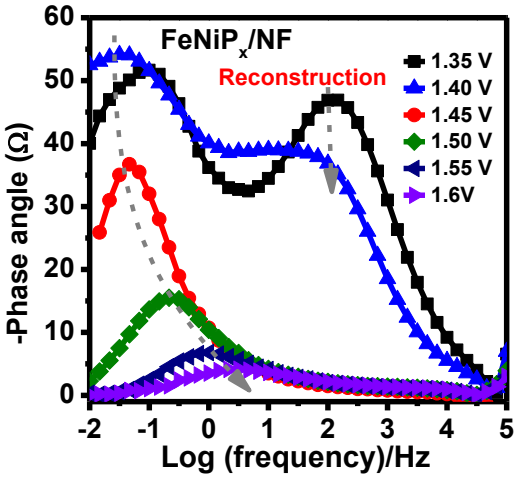

Fig. S15 Bode plot for $FeNiP_x$/NF at different potentials (vs RHE) during in-situ electrochemical OER process.

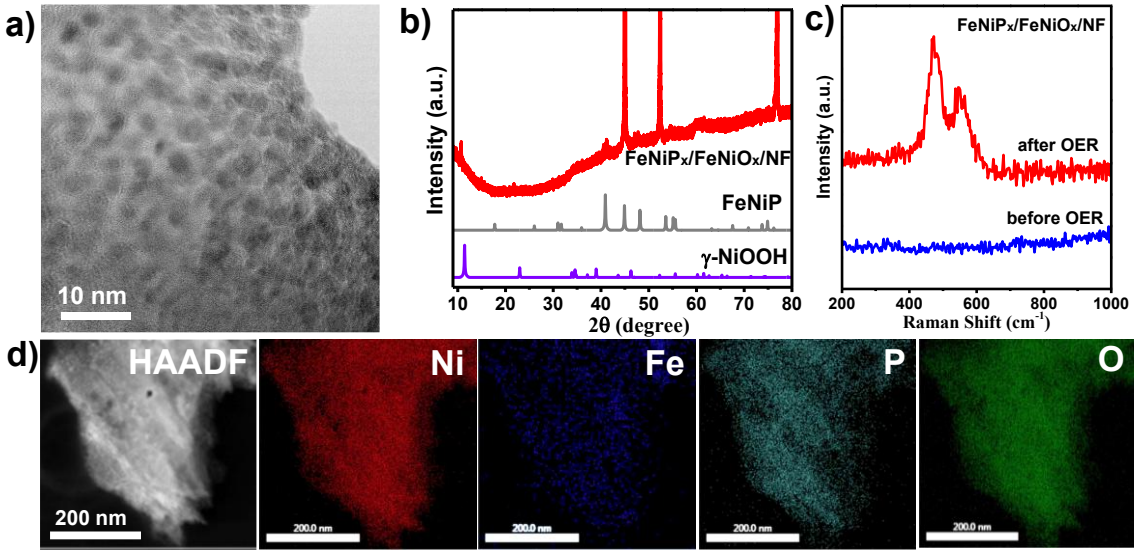

Fig. S16 $FeNiP_x/FeNiO_x/NF$ characterization after OER: (a) HR-TEM image, (b) PXRD, (c) Raman spectra, and (d) STEM image with corresponding elemental mappings.

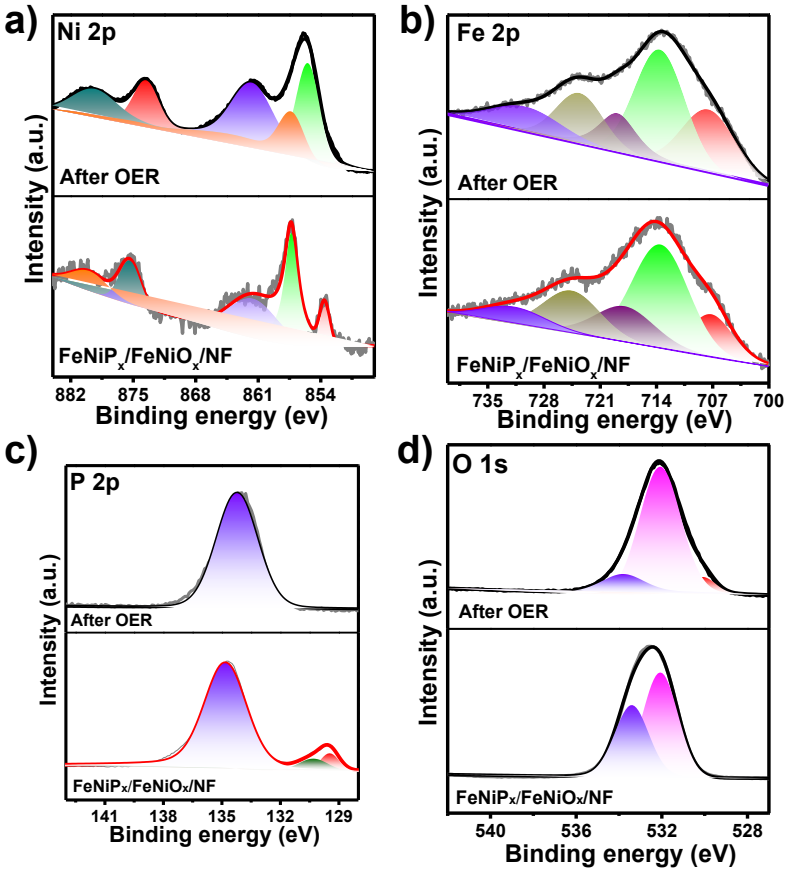

Fig. S17 XPS spectra of $FeNiP_x/FeNiO_x/NF$ after OER: (a) Ni 2p, (b) Fe 2p, (c) P 2p and (d) O 1s.

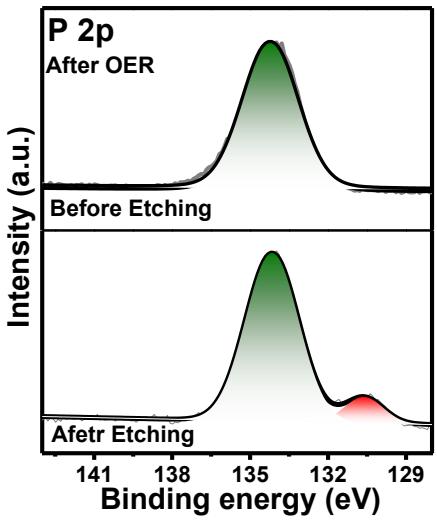

Fig. S18 XPS spectra of $FeNiP_x/FeNiO_x$/NF after OER: before Ar spurting and after Ar spurting.

Table 1 OER performance comparison of the as synthesized electrocatalyst with other electrocatalysts

Catalysts	**Substrate**	**Tafel Slope mV/dec**	**η_{100} (mV)**	**Synthesis process**	**References**
FeNiPx/ FeNiOx/NF	**NF**	**42**	**220**	**Hydrothermal treatment followed by phosphidation**	**This work**
$NiSe_2$-Ni_2P/CC	CC	46.5	270	Co-crystallization involving in situ transformation of amorphous Ni−P through gas−solid reactions and selenization	Y. Wang, R. Yin, L. Yuan, X. Guo, X. Zheng, Q. Fan, Z. Duan, Y. Liu, J. Zhang and S. Xiong, ACS Energy Lett., 2025, **10**, 837
CeCoFeP@MXene	NF	58.4	266	Synthesis of CeCoLDH@MXene, followed by PB modification	Y.-H. Pan, S. Perumal, M. Sakthivel, S.-N. Lin, M.-H. Yeh, W.-Y. Yu and K.-C. Ho, *Chem. Eng. J.,* 2025, **515**, 163888.
Mn-Co-Fe-P	NF	43.75	279	Hydrothermal synthesis followed by phosphidation	F. Wang, Z. Pei, Z. Xu, T. Qin, X. Ouyang, D. Li, Y. Hou and X. Guo, Adv. Sci., 2025, **12**, 2417521.
Ru_x-Co_3O_4	--	68.3	311 (ir-corrected)	Impregnation solution was of Ru in Co_3O_4 followed by calcination	Y. Zhou, Y. Mao, C. Ye, Z. Wang, S. Wei, J. V. Kennedy, Y. Zhao, H. Yang, B. C. C. Cowie and G. I. N. Waterhouse, *Adv.Energy Mater.,* 2025, **15**, 2500700.
Mo-CoP/NC	NF	46.3	~300	Hydrothermal synthesis followed by phosphorating	W. An, Z. Liu, T. Shen, Y. Du, C. Huang, B. Duan, C. Wang, G. Huang, Y. Yan and S. Xu, *ACS*

					Catalysis, 2025, ***15***, 10358-10371.
MoP_2−NiCoP/NF	NF	47.6	233 (ir-correc ted)	Hydrothermal synthesis followed by phosphorating	L. Qian, H. Hu, Y. Zheng, Y. Zhu, Z. Yuan, Y. Dai, T. Zhang, D. Yang and F. Qiu, *Inorg. Chem.,* 2024, **63**, 1 682–1691.
$FeNi_2P$–C/P-rGA	NF	56.4	315	Hydrothermal and phosphating treatments	X. Yu, Y. Li, C. Pei, Z. Zhao, Y. Lu, W. Zhou, D. Guo, W. Li, J. K. Kim and H. S. Park, *Inorg. Chem.,* 2024, **63**, 18945.
NiPx-FeOx	--	--	~400	Thermal decomposition of $Fe(CO)_5$ in the presence of the NiP_x nanoparticles followed by oxidation	R. H. Manso, J. Hong, W. Wang, P. Acharya, A. S. Hoffman, X. Tong, F. Wang, L. F. Greenlee, Y. Zhu, S. R. Bare and J. Chen, *Chem. Mater.,* 2024, **36**, 6 440–6453
Ni_2P–$NiMoO_x$/NF	NF	60.1	188	Hydrothermal synthesis followed by phosphidation	J.-T. Ren, L. Chen, H.-Y. Wang, W.-W. Tian, X.-L. Song, Q.-H. Kong and Z.-Y. Yuan, *ACS Catal.,* 2023, **13**, 97 92
NiFeO-CeO_2/NF	NF	46.6	~170	Hydrothermal synthesis followed by phosphidation & CV activation	H. Zhang, Z. Bi, P. Sun, A. Chen, T. Wagberg, X. Hu, X. Liu, L. Jiang and G. Hu, *ACS Nano,* 2023, **17**, 16008.
Co3Fe/Ce0.025	--	47.25	320	Hydrothermal followed by phosphorating of the powder	X. Z. Song, T. Zhang, Y. H. Zhao, J. C. Ni, Y. Pan, Z. Tan and X. F. Wang, *Inorg. Chem.,* 2023, **62**, 8 347.

CoNiLDH/FeOOH	CC	60	~450	Growth of CoNiLDH over MOF surface with Fe impregnation	P. Zhao, S. Fu, Y. Luo, C. Peng, L. Cheng and Z. Jiao, *Small,* 2023, **19**, 2305241.
Ni_2P@ FePOxHy	--	43	~270 (ir-corrected)	Various steps of hydrothermal and phosphidation	A. Meena, P. Thangavel, D. S. Jeong, A. N. Singh, A. Jana, H. Im, D. A. Nguyen and K. S. Kim, *Appl. Catal., B* 2022, **306**, 121127.
Co@CoFe–P NBs	--	26.94	310	Through reconstruction of ZIF-67@CoFe–PB	Y. Zhao, N. Dongfang, C. A. Triana, C. Huang, R. Erni, W. Wan, J. Li, D. Stoian, L. Pan, P. Zhang, J. Lan, M. Iannuzzi and G. R. Patzke, *Energy Environ. Sci.,* 2022, **15**, 727.
S-Doped Nickel Iron Phosphides	NF	43.1	--	Synthesis of MOF/cc followed by phosphidation	S. Li, L. Wang, H. Su, A. Hong, Y. Wang, H. Yang, L. Ge, W. Song, J. Liu, T. Ma, X. Bu and P. Feng, *Adv. Funct. Mater.,* 2022, **32**, 2200733.
NiFe LDH/FeOOH	NF	69.8	286.2	Ultrasonication of precursors in D.I. followed by electrodeposition	K. Jiang, W. J. Liu, W. Lai, M. L. Wang, Q. Li, Z. L. Wang, J. J. Yuan, Y. L. Deng, J. Bao and H. B. Ji*, Inorg. Chem.,* 2021, **60**, 17371.
NiFe-LDH	carbon	37	~390	Sol-gel method of nanoparticle synthesis	H. Koshikawa, H. Murase, T. Hayashi, K. Nakajima, H. Mashiko, S. Shiraishi and Y. Tsuji, *ACS*

					Catal., 2020, **10**, 1886.
Ni_2P-Fe_2P	NF	58	261	Hydrothermal hydroxide formation followed by metal exchange with Fe and high temperature phosphidation	L. Wu, L. Yu, F. Zhang, B. McElhenny, D. Luo, A. Karim, S. Chen and Z. Ren, *Adv. Funct. Mater.,* 2021, **31**, 2006484
FeNiP/NCH	Carbon	68	~350 (ir-corrected)	Synthesis of MOF followed by its pyrolysis	Y.-S. Wei, M. Zhang, M. Kitta, Z. Liu, S. Horike and Q. Xu, *J. Am. Chem. Soc.,* 2019, **141**, 7906.
CoP@a-CoOx	--	67	~300 (ir-corrected)	Solvothermal synthesis followed by phosphidation	J. Yu, Y. Zhong, X. Wu, J. Sunarso, M. Ni, W. Zhou and Z. Shao, *Adv. Sci.*, 2018, **5**, 1800514.
FeP/Ni_2P	NF	22.7	~240	Chemical vapour deposition followed by phosphidation	F. Yu, H. Zhou, Y. Huang, J. Sun, F. Qin, J. Bao, W. A. Goddard, S. Chen and Z. Ren, *Nat. Commun.,* 2018, **9**, 2551.
FeOOH/Co/FeOOH	NF	--	320	Electrodeposition	J. X. Feng, H. Xu, Y. T. Dong, S. H. Ye, Y. X. Tong and G. R. Li, *Angew. Chem., Int.Ed.,* 2016, **55**, 3694